




# Full optical SESAM characterization methods in the 1.9 to 3- $\mu\text{m}$ wavelength regime

JONAS HEIDRICH,<sup>\*</sup>  MARCO GAULKE,  BEHCET OZGUR ALAYDIN,  MATTHIAS GOLLING, AJANTA BARH,  AND URSULA KELLER 

*Department of Physics, Institute for Quantum Electronics, ETH Zürich, 8093 Zürich, Switzerland*  
*\*hejonas@phys.ethz.ch*

**Abstract:** Semiconductor saturable absorber mirrors (SESAMs) are widely used for mode-locking of various ultrafast lasers. The growing interest for SESAM-modelocked lasers in the short-wave infrared and mid-infrared regime requires precise characterization of SESAM parameters. Here, we present two SESAM characterization setups for a wavelength range of 1.9 to 3  $\mu\text{m}$  to precisely measure both nonlinear reflectivity and time-resolved recovery dynamics. For the nonlinear reflectivity measurement, a high accuracy ( $<0.04\%$ ) over a wide fluence range (0.1–1500  $\mu\text{J}/\text{cm}^2$ ) is achieved. Time-resolved pump-probe measurements have a resolution of about 100 fs and a scan range of up to 680 ps. Using the two setups, we have fully characterized three different GaSb-SESAMs at an operation wavelength of 2.05  $\mu\text{m}$  fabricated in the FIRST lab at ETH Zurich. The results show excellent performance suitable for modelocking diode-pumped solid-state and semiconductor disk lasers. We have measured saturation fluences of around 4  $\mu\text{J}/\text{cm}^2$ , modulation depths varying from 1% to 2.4%, low non-saturable losses ( $\sim 0.2\%$ ) and sufficiently fast recovery times ( $< 32$  ps). The predicted influence of Auger recombination in the GaSb material system is also investigated.

© 2021 Optical Society of America under the terms of the [OSA Open Access Publishing Agreement](#)

## 1. Introduction

Semiconductor saturable absorber mirrors (SESAMs) have been widely used for ultrashort pulse generation for more than 25 years [1,2]. There is a strong interest for SESAMs operating in the short-wave infrared (SWIR) and mid-infrared (mid-IR) for self-starting, passive modelocking [3–7] and for dual-comb modelocking [8,9] with lidar and spectroscopy applications. For example the 2- $\mu\text{m}$  region is very appropriate for CO<sub>2</sub> spectroscopic sensing [10] with a high transmission in air [11]. In order to precisely characterize the SESAM parameters, we have developed both a nonlinear reflectivity and a pump-probe setup covering a spectral range from 1.9 to 3  $\mu\text{m}$ . We demonstrate the precision of the optical characterization with several high-performance 2- $\mu\text{m}$  SESAMs grown in the FIRST lab at ETH Zurich.

A SESAM [1] typically consists of a highly reflecting distributed Bragg reflector (DBR) with a semiconductor saturable absorber section, which can be a bulk semiconductor or an epitaxial layer containing quantum wells (QWs) or quantum dots. The saturable absorber has the characteristic to saturate at sufficiently high pulse fluence (pulse energy per area) which increases the reflectivity of the device. The right combination of SESAM parameters are essential to obtain stable modelocking [12–14]. The SESAMs are characterized by the saturation fluence, modulation depth, non-saturable losses and a rollover parameter together with the recovery time of the absorber.

The nonlinear reflectivity measurement technique has been developed in the near-IR regime achieving an accuracy below 0.02% [15–18]. We transferred this know-how into the infrared regime for the first-time with comparable accuracy (Fig. 1). It is important to characterize SESAMs with low modulation depths of a few percent and with nonsaturable losses of less than

1%. Such SESAMs are required for example for modelocking optically pumped semiconductor lasers (i.e. VECSELs and MIXSELs) [19,20], dual-comb modelocked solid-state lasers [21] and high repetition rate lasers [22]. The high dynamic fluence range of more than three orders of magnitude allows for a reliable measurement of the rollover parameter. The pump-probe setup, tunable over the same wavelength range, determines the recovery times of the SESAM. The recovery time of 2- $\mu\text{m}$  SESAMs have been measured before [23], but to our knowledge the required high-precision nonlinear reflectivity measurements have been missing.

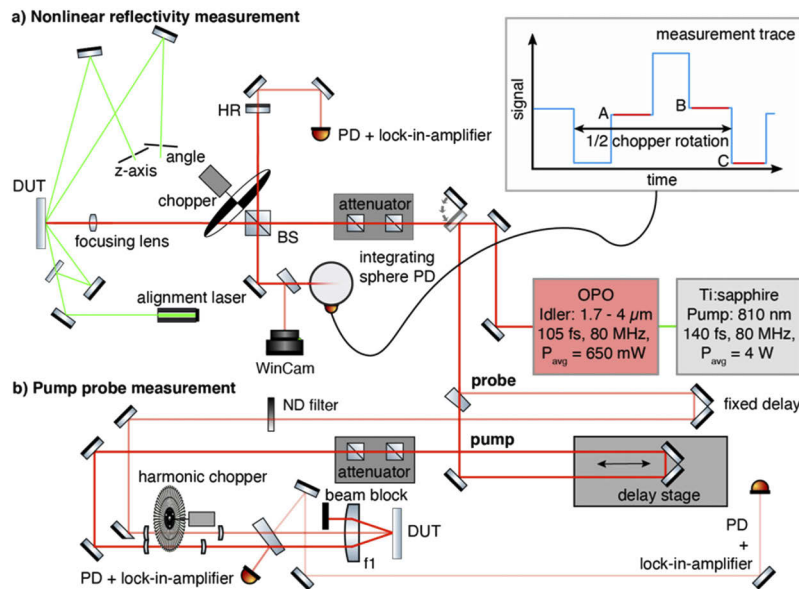


**Fig. 1.** Full SESAM characterization for an infrared wavelength range of 1.9–3  $\mu\text{m}$ : a) nonlinear reflectivity and b) recovery dynamics. The SWIR/mid-IR laser source is a tunable femtosecond optical parametric oscillator (OPO) pumped by a modelocked Ti:sapphire laser. The full power of the idler beam is used either for the nonlinear reflectivity or the pump-probe measurement using a flip mirror for guiding the beam accordingly. DUT: device under test (e.g. SESAM to be characterized), BS: beam splitter, PD: photodetector, HR: high reflector.

In section 2 we describe the measurement setups as shown in Fig. 1 with the alignment and calibration procedure required for high-precision measurements. In section 3 we describe the 2- $\mu\text{m}$  SESAM structures and the obtained characterization results.

## 2. Measurement setups

For both, the nonlinear reflectivity and time-resolved measurement setup, we use a commercial broadband femtosecond (fs) optical parametric oscillator (OPO) (i.e. Radiantis Oria IR XT) pumped by a femtosecond Ti:sapphire laser operating at 810 nm as shown in Fig. 1. The OPO idler beam can be tuned from 1.7 – 4  $\mu\text{m}$  with around 100-fs pulse duration at a repetition rate of 80 MHz and a maximum average output power of 650 mW. Broadband SWIR optics are used in both setups such as metallic mirrors, broadband polarizers, mid-IR coated calcium fluoride lenses and beam splitters. In addition, we use exchangeable extended InGaAs or InAsSb photodetectors. Due to the OPO's robustness against back-reflections, no optical isolator is needed in contrast to prior approaches in the near-IR regime [15,16]. Isolators typically have the disadvantage of high losses, high dispersion, a narrow bandwidth of transmission and high cost. Our selection of optics enables a broadband characterization of SESAMs from 1.9  $\mu\text{m}$  to 3  $\mu\text{m}$  operating wavelength. The effect of dispersive pulse broadening within the two setups are negligible. At the device

under test (DUT) position a pulse duration below 120 fs is estimated for both setups with a high-dynamic fluence range over more than 3 orders of magnitude and an upper limit exceeding intracavity conditions for SESAM modelocking. A flip mirror right after the OPO allows for directing the beam with full power either into the nonlinear reflectivity or the pump-probe setup. Further details on the setups are discussed in the following sub-sections.

### 2.1. Nonlinear reflectivity measurement setup

The nonlinear reflectivity measurement setup (Fig. 1(a)) is designed to measure the nonlinear reflectivity of SESAMs and is based on the principle given by Maas et al. [16]. The OPO has sufficient output power (max. 650 mW) to operate the setup over a wavelength range from 1.9 to 3  $\mu\text{m}$ . The optics are chosen carefully to cover a high dynamic fluence measurement range of more than  $10^3$ . The power of the OPO beam, which determines the fluence on the DUT, is adjusted during the measurement using a variable and a fixed wire grid polarizer. The variable polarizer is mounted in a high-precision (60  $\mu\text{rad}$ ) stepper-motor stage. Wire grid polarizers have the advantage of a high extinction ratio of  $10^5:1$  over the full wavelength range and excellent beam pointing stability when rotated. The subsequent reflection measurement part of the setup has a Michelson-interferometer geometry where the beam is split into a probe and a reference arm.

We use a broadband (1–6  $\mu\text{m}$ ) coated calcium fluoride beam splitter to divide the OPO beam into two parts that are sequentially blocked with a 2-slot chopper blade at a frequency of 110 Hz. One part is reflected by a high reflecting (HR) reference mirror with a reflectivity  $> 99.5\%$ . The leakage of the reference mirror is focused onto a reference photodiode. The signal is measured with a lock-in amplifier locked at 110 Hz and used for fluence monitoring. The SESAM under test is probed with the focused sample beam. By selecting an appropriate focusing lens, both low fluences down to  $0.1 \mu\text{J}/\text{cm}^2$  and high fluences up to  $1500 \mu\text{J}/\text{cm}^2$  can be obtained. These fluences are sufficient to probe both the linear reflectivity (at low fluence level) and the inverse saturable absorption regime (at high fluence level) of the GaSb-SESAMs under test. The reflected beams from the reference mirror (HR) and the sample are recombined at the beam splitter and sent into an integrating sphere photodetector with the advantage of being independent from beam pointing instabilities and spatial inhomogeneities of the photodetector. A small part of the signal beam (reflected from a flip-wedge) can be directed towards a microbolometer based mid-IR camera (DataRay WinCamD-IR-BB), for imaging the reference and sample beam, which helps to improve alignment.

The recorded signal is dynamically amplified using a low-noise current amplifier (from 20 nA/V to 1 mA/V) together with a 24-bit analog-to-digital converter sampling at 50 kS/s. An algorithm sets the number of recorded measurement cycles (see measurement trace in Fig. 1(a)) depending on the noise level of a pre-measurement. In order to achieve a similar error for every measurement point, between 200 (low-noise case) to 500 (high-noise case) measurement cycles are chosen. The SESAM reflectivity for each cycle  $R = (A - C)/(B - C)$  is calculated by synchronously measuring the signal from the sample and the reference arm, referred as level A and B. The subtraction of level C removes the photodiode offset. Averaging over the sampling points of each level minimizes the detector and amplifier noise, whereas averaging over the reflectivity value of each cycle reduces the influence of power fluctuations of the OPO, which typically happen on a timescale of seconds. Using this method with an optimized algorithm, a precise reflectivity measurement for 30 fluence values is performed in just 7 minutes.

#### 2.1.1. Alignment and calibration

The setup is calibrated prior to a set of nonlinear measurements of SESAMs. The rotation angle of the polarizer is referenced to the power at the DUT position and the power at the reference photodiode. To precisely determine the fluence on the DUT, the focal spot size is measured at the

DUT position by using a scanning slit profiler (DataRay Beam'R2). Subsequently, an absolute reflectivity calibration is performed using a second dielectric HR mirror placed at the focal position of the focusing lens. This HR mirror has a flat reflectivity of  $R = 99.9\%$  over the entire spectrum of the OPO (Fig. 3(b)), and we can calibrate the setup to obtain the absolute reflectivity over the targeted fluence range. A sanity check is performed by measuring the reflectivity of the same HR (instead of a SESAM) using the reference reflectivity. This should result in a flat response over the full fluence range at the DUT. The result of this high precision measurement reveals a reflectivity of  $R = 99.95\%$  with a standard deviation of  $\sigma \leq 0.04\%$ . It is shown together with the SESAM measurement results in section 3 Fig. 3(b) (yellow dotted). To briefly emphasize this high accuracy is only achieved by minimizing beam pointing fluctuations due to moving parts, low-noise amplification of robust integrating sphere photodetectors and a sophisticated averaging method.

To maintain this level of precision when placing a SESAM at the focal spot of the beam, a three-step alignment procedure is performed. First, a rough alignment of the angular and z-position of the sample is done with a green alignment laser (see Fig. 1(a)) [16]. In a second step, the camera is used to match the beam profiles of the sample and reference arm by adjusting the focus position of the SESAM. With this approach the SESAM can be placed exactly in the beam waist after the focusing lens when the reflected beam from the sample matches the collimated beam from the reference mirror. For a final fine adjustment step of the DUT position, the incident fluence is set (by using the variable attenuator) slightly below the saturation fluence on the rising reflectivity slope of the nonlinear reflectivity curve (as shown in Fig. 3(b)) such that any increase in fluence should result in a higher value of reflectivity. A live SESAM reflectivity readout is then used to maximize the reflectivity by fine tuning the DUT position in the focus.

## 2.2. Time resolved measurement setup

Absorber recovery dynamics of a SESAM is an important characteristic and plays a crucial role in stabilizing SESAM modelocking. We have developed a mid-IR pump-probe setup with the same polarization using the femtosecond OPO for measuring the recovery times of our GaSb-SESAMs. The OPO beam is guided into the pump-probe measurement setup using a flip mirror as it is shown in Fig. 1(b). The fraction of reflected beam from an uncoated calcium fluoride wedge is used as the probe and the transmitted higher intensity beam serves as the pump. While the probe beam has a fixed path length, the pump beam is aligned to a retro reflector mounted on a 204 mm long high-precision linear encoder stage (PI M-521). This enables for a long delay scanning window of up to 680 ps. Since the stage has a spatial resolution of  $0.1 \mu\text{m}$  corresponding to a temporal resolution of 0.66 fs, it is well suited for pump-probe experiments with 100-fs pulses. A variable attenuator (cross-polarizer) is used to control the pump fluence on the DUT, whereas a filter wheel containing various neutral-density (ND) filters is used to control the probe fluence.

We have used a single 42/30-slit harmonic chopper wheel to modulate the pump and probe beam at different frequencies. Both beams are focused at the position of the chopper blade to achieve a clear modulation. Afterwards, the probe beam is collimated with a lens of longer focal length, resulting in a larger beam diameter for the probe beam compared to the collimated pump beam.

The pump and probe beam are aligned parallel to each other throughout this part of the setup, so that one single aspheric lens ( $f_1$ , in Fig. 1(b)) can be used for focusing both beams on the DUT. This has the advantage that both beams precisely overlap at the focal position. Prior to this focusing lens, a calcium fluoride wedge is used to partially reflect the pump beam to control the pump fluence and monitor the OPO power. The focusing lens is placed such that the probe beam passes exactly through its center whereas the pump beam is horizontally shifted and passes through a peripheral region. This ensures an excellent beam pointing stability of the reflected probe signal from the DUT while adjusting its position at the focus. Moreover, this geometry

facilitates a clear separation of the reflected pump light. The larger size of the probe beam compared to the pump beam at the input of the lens ( $f_1$ ) ensures a smaller focused spot size for the probe beam and a complete spatial overlap with the pump spot at the focus position on the DUT. The reflected probe light of a SESAM under test is detected using a self-assembled large area extended InGaAs photodiode with a lock-in amplifier.

### 2.2.1. Alignment and measurement

In order to characterize the SESAMs, the wavelength of OPO is set to 2050 nm (see SESAM details in section 3). A scanning slit profiler (DataRay Beam'R2) is used to separately measure the spot size of the pump and probe beam, and to optimize their spatial overlap. The focus of the probe beam has a diameter of 40  $\mu\text{m}$  at the DUT position and is overlapped with the elliptical pump beam of dimension 62  $\mu\text{m}$  x 93  $\mu\text{m}$ . The pump and probe fluences are calculated by measuring their respective powers at the focal position. The fluence ratio between the pump and probe beam is adjusted according to the saturation behavior of the SESAM, which is at least 100:1 for our case in order to prevent any saturation originating from the probe. These fluences are controlled using the attenuator and ND filter as mentioned earlier.

The pump-probe signal is the direct reflectivity change  $\Delta R/R$  of the SESAM. As the reflectivity change is caused by a pump pulse and detected with a probe pulse, the pump-probe signal is found in the frequency beating of the two beams. Generally, this signal intensity is much smaller than the incoming probe intensity. As a consequence, the signal is measured with lock-in detection. The harmonic chopper modulates the amplitude of the pump beam at a frequency of 2.55 kHz and the probe beam at 1.821 kHz. The signal is detected at the difference frequency of 729 Hz rather than at the higher sum frequency of the beating, as the difference frequency spans more octaves with the probe modulation frequency of 1.821 kHz. This enables a more effective electronic filtering.

## 3. Results and discussion of 2.05- $\mu\text{m}$ SESAMs

We have fully characterized three new GaSb SESAMs fabricated in the FIRST clean room facility of ETH Zürich. The antiresonant SESAM designs used in this work are shown Fig. 2. All samples are grown with molecular beam epitaxy (MBE) on (100) n-type GaSb substrates. A GaSb buffer layer is followed by a 20 pair GaSb/ $\text{AlAs}_{0.08}\text{Sb}_{0.92}$  lattice matched DBR grown at 525  $^{\circ}\text{C}$ . The 11.5 nm thick  $\text{In}_{0.27}\text{Ga}_{0.73}\text{Sb}$  QWs are grown at 455  $^{\circ}\text{C}$  and embedded in a GaSb barrier layer with a QW spacing of 10 nm.

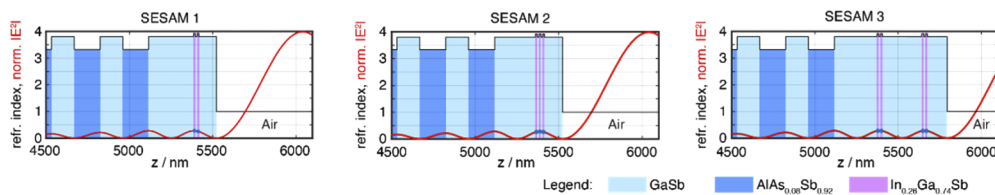


**Fig. 2.** Three different 2.05- $\mu\text{m}$  InGaSb/GaSb quantum well (QW) SESAM designs. The refractive index variation (black) and the electric field intensity standing wave pattern normalized to 4 in air (red) are plotted over the thickness of the structures. The position of the QWs is marked with blue dots on the antinodes of the electric field intensity. Two, three and four QWs are grown in SESAM 1, SESAM 2 and SESAM 3, respectively. The semiconductor compounds are labeled with different colors (see Legend) for each area of refractive index.

At first a low intensity spectral reflectivity measurement (Varian Cary 5E) over the stop band of the SESAMs is carried out and shown in Fig. 3(a). The stop band is defined by the lower



high-reflecting GaSb/AlAs<sub>0.08</sub>Sb<sub>0.92</sub> DBR and reveals a broad stop-band bandwidth of around 200 nm. Based on the spectral position of the absorption dip around 2.05  $\mu\text{m}$ , the nonlinear reflectivity and pump-probe characterization is performed at a center wavelength of 2.05  $\mu\text{m}$ . In addition, Fig. 3(a) reveals the photoluminescence (PL) spectrum (Bruker Vertex 80 PL II) over the identical wavelength range. The peaks of the PL signal originating from the QWs in the SESAM structure match the absorption band edge at 2.05  $\mu\text{m}$ . This PL peak intensity is about two orders of magnitude lower than the PL signal originating from the GaSb substrate at 1.7  $\mu\text{m}$ , which indicates strong non-radiative decay mechanisms of excited carriers within the QWs.

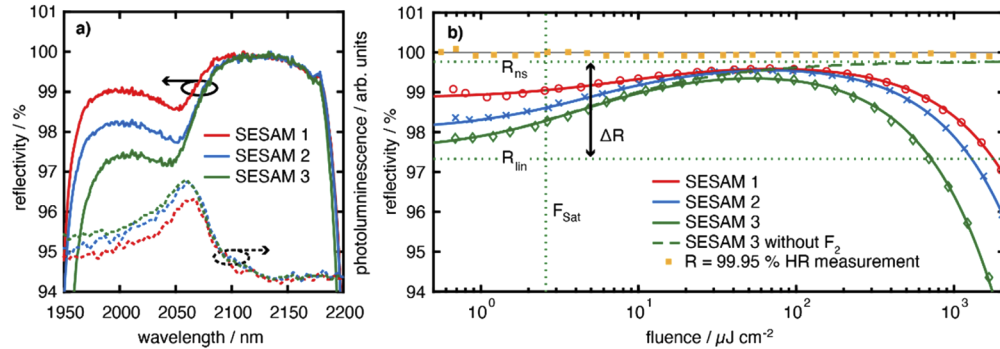


**Fig. 3.** (a) Low intensity spectral reflectivity and photoluminescence (PL) measurement of the investigated SESAMs. The reflectivity is plotted over the wavelength range of the stop-band of the lower DBR. The PL intensity peak matches the QW absorption dip of the spectral reflectivity measurement. (b) Nonlinear reflectivity measurement results. The reflectivity is plotted over the fluence on the SESAM. Measurement results are plotted with a fit for all three SESAMs according to Eq. (2). The green dashed line shows the fit for SESAM 3 for no inverse saturable absorption e.g.  $F_2 \rightarrow \infty$ . The green dotted lines indicate the reflectivity  $R_{lin}$  and  $R_{ns}$  as well as the saturation fluence  $F_{Sat}$  for SESAM 3. The sanity check measurement of the HR mirror (yellow squares) used for the calibration gives a high precision reflectivity of  $R = 99.95\% \pm 0.04\%$  over the full dynamic range.

The nonlinear reflectivity measurement of the three different SESAMs is shown in Fig. 3(b), where the reflectivity is plotted as a function of incident fluence on the DUT. It increases with fluence up to a point where induced absorption processes set in. Hence, the reflectivity decreases again at higher fluence values. The model function for the nonlinear reflectivity of a SESAM using a rate equation model for a two-level system is given as follows [15]:

$$R^{FlatTop}(F) = R_{ns} \frac{\ln \left( 1 + \left( \frac{R_{lin}}{R_{ns}} \right) (\exp(F/F_{Sat}) - 1) \right)}{F/F_{Sat}} \cdot \exp \left( -\frac{F}{F_2} \right). \quad (1)$$

This determines the nonlinear reflectivity as a function of fluence ( $F$ ) of a SESAM probed with a flat top beam, with  $F_{Sat}$  the saturation fluence,  $R_{lin}$  the unsaturated reflectivity in the linear regime,  $R_{ns}$  the highest reflectivity limited by nonsaturable losses and  $F_2$  the rollover parameter.  $F_{Sat}$  is determined as the fluence where the reflectivity reduces to  $1/e$  of its maximum. The nonsaturable losses originate from any linear absorption and scattering at impurities in the semiconductor. Thus, the maximum reachable reflectivity of a SESAM is lower than the theoretical reflectivity of 100%. Beyond that, induced absorption causes an inverse saturable absorption resulting in a strong decrease in reflectivity at higher fluences [24]. This rollover becomes more important with shorter pulses due to two-photon absorption and is quantified using the rollover parameter. When applying this model, we assume that no considerable relaxation takes place over a pulse duration and we neglect standing wave effects. Equation (1) has an additional modification for a

Gaussian beam profile [15]

$$R^{\text{Gauss}}(F_P) = \frac{1}{2F_P} \int_0^{2F_P} R^{\text{FlatTop}}(F) dF, \quad (2)$$

where the pulse fluence  $F_P = E_P/(\pi w^2)$  is calculated from the pulse energy  $E_P$  and the beam waist  $w$ .

Table 1 shows the key parameters obtained from fitting the reflectivity function  $R^{\text{Gauss}}(F_P)$  with the measurement data of each SESAM. The low saturation fluence between 2.6 and 5.0  $\mu\text{J}/\text{cm}^2$  is expected from a SESAM design with QWs placed in the antinodes of the standing wave profile. It is possible to achieve higher saturation fluences for a SESAM by adapting the material and structural design [5,25]. The modulation depth increases with the number of QWs due to the higher number of carriers excited to saturate the SESAM. This is also found in the linear reflectivity curve in Fig. 3(a). The investigated GaSb SESAMs show low non-saturable losses of around 0.2%, which indicates excellent growth quality of the semiconductor epilayers. The crystalline quality is confirmed using structural analysis like XRD rocking curve and differential interference contrast microscopy. Since the rollover occurs at lower fluences for an increasing number of QWs, there is significant induced higher order absorption in the QW layers of the structure [26]. This can be explained with the inverse dependence of  $F_2$  on the two photon absorption (TPA) coefficient [15] which becomes more dominant in the fs-regime [24]. The TPA coefficient for GaSb and  $\text{In}_{0.27}\text{Ga}_{0.73}\text{Sb}$  can be estimated as 125 cm/GW and 775 cm/GW, respectively [27,28]. The high bandgap material  $\text{AlAs}_{0.08}\text{Sb}_{0.92}$  results in negligible TPA in these layers. Hence, the presence of more material with a high TPA coefficient shifts the rollover to lower fluences.

**Table 1. SESAM parameters obtained from the nonlinear reflectivity measurement at 2.05  $\mu\text{m}$**

	SESAM 1	SESAM 2	SESAM 3
QWs	2	3	4
Saturation fluence ( $\mu\text{J}/\text{cm}^2$ )	5.0	2.9	2.6
Modulation depth (%)	1.0	1.8	2.4
Non-saturable losses (%)	0.18	0.15	0.23
Rollover parameter ( $\text{mJ}/\text{cm}^2$ )	70.6	50.8	29.3

The recovery dynamics of the SESAMs are investigated using the demonstrated pump-probe setup with a pump fluence set to 32.2  $\mu\text{J}/\text{cm}^2$ . Since the pump-probe signal is determined by the change in reflectivity, the pump fluence is set to a value below the SESAM rollover point. This is also the condition where a saturable absorber is ideally operated in the laser cavity [14]. The fluence of the probe beam is set to a small value of 0.13  $\mu\text{J}/\text{cm}^2$  in order to prevent any saturation effects from the probe pulse. The pump-probe measurements of the SESAMs are plotted in Fig. 4(a). Time zero is set for the pump and probe pulse overlap. We subtract the small background by averaging the signal before the temporal overlap and normalize the signal to its maximum value. A trend towards a better signal-to-noise ratio is found for a SESAM with higher modulation depth (e.g. for SESAM 3, green solid line). The pump-probe response shows a large fast component, which drops to  $\sim 30\%$  of its initial value, and a subsequent slow component  $> 10$  ps.

In order to quantify the temporal response of the SESAMs, we apply the model for the total recombination rate according to section 10.10 in [29]. The first order term in the model describes non-radiative Shockley-Read-Hall (SRH) recombination (also called trap-assisted recombination), the second order term describes the radiative bi-molecular recombination mechanism and the third order term describes Auger recombination. In the subsequent analysis, we neglect the

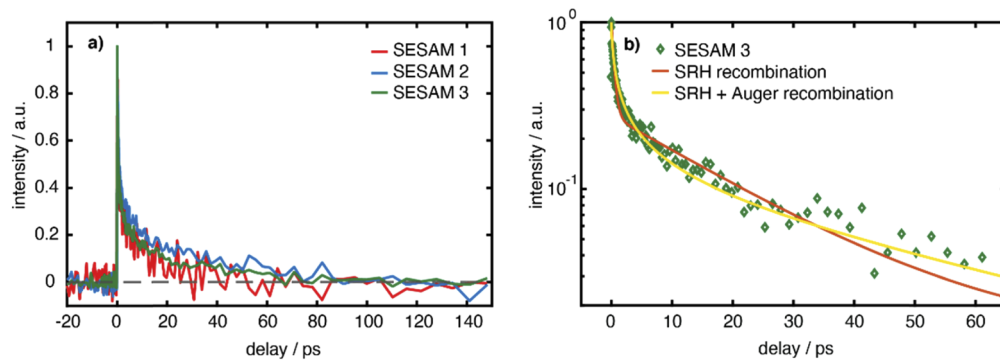


**Fig. 4.** (a) Pump-probe measurement results of the investigated SESAMs. (b) Different models fitted to the pump-probe data of SESAM 3. The orange curve contains only non-radiative band impurity Shockley-Read-Hall (SRH) recombination. The yellow curve includes an additional Auger recombination channel.

radiative bi-molecular recombination mechanism as the measured PL signal (Fig. 3(a)) from the QWs is strongly reduced as discussed above.

When considering only SRH recombination the conventional bi-exponential decay function

$$\Delta R(\tau) = A e^{-\tau/\tau_1} + (1 - A) e^{-\tau/\tau_2}, \quad (3)$$

is deducted as it used e.g. in [30]. Here  $A$  is the weighting factor between the two time constants  $\tau_1$  and  $\tau_2$ . Equation (3) is fitted with the measurement data shown in Fig. 4(a). The obtained fit parameters are given in Table 2.

**Table 2. SESAM parameters measured using the pump-probe setup at 2.05  $\mu\text{m}$**

	SESAM 1	SESAM 2	SESAM 3
$A$ (%)	71	71	74
$\tau_1$ (ps)	0.56	0.73	0.47
$\tau_2$ (ps)	16	32	20

All samples exhibit a large weighting factor  $A > 70\%$  together with a very short time constant  $\tau_1 < 1$  ps. This faster relaxation relies on intraband thermalization of excited carriers, whereas the second slower relaxation happens due to the trap-assisted recombination in the QWs [1]. In comparison to 1- $\mu\text{m}$  SESAMs the measured second time constant can be considered fast. Thus, our SESAMs reveal recovery timescales suitable for ultra-short pulse generation [12,31].

Although, Eq. (3) provides a satisfactory fit to the measured data and the obtained time scales are sufficiently accurate with regards to modelocking, the additional effect of Auger recombination on the recovery dynamics can be investigated as well. The Auger recombination is expected to be enhanced in low-bandgap materials like GaSb and InGaSb [32]. Thus, we use the pump-probe data of SESAM 3 for a comparison of a pure SRH band impurity recombination with a model considering an additional Auger recombination channel.

The result of this comparison is shown in Fig. 4(b). The decay mechanism considering both SRH and Auger recombination reveals a better fit (yellow solid) for the slow recovery dynamics with a 10% smaller squared norm of the residual compared to pure SRH band impurity recombination. Thus, we can conclude that Auger-recombination is present in GaSb-SESAM structures but this decay channel remains difficult to be quantified.



#### 4. Conclusion and outlook

We have demonstrated full SESAM characterization with an unprecedented accuracy in the spectral region of 1.9  $\mu\text{m}$  to 3  $\mu\text{m}$ . It consists of a nonlinear reflectivity measurement setup reaching an accuracy  $< 0.04\%$  over a high dynamic fluence range of more than  $10^3$ , and a time resolved measurement setup, both operated with a broadband femtosecond OPO system.

A full characterization of newly grown SESAMs for a center wavelength of 2.05  $\mu\text{m}$  show excellent performance for passive modelocking of diode-pumped solid-state and semiconductor lasers: low saturation fluences of a few  $\mu\text{J}/\text{cm}^2$  and extremely low nonsaturable losses ( $\sim 0.2\%$ ). The number of QWs, can be used to adjust the modulation depth from 1 to 2.4%. The recovery times between 10 and 30 ps are ideally suited for self-starting soliton modelocking [12]. The contribution of Auger-recombination for GaSb based SESAMs could be demonstrated. Such a full characterization of SESAMs is key for the development of state-of-the-art ultrafast lasers in the SWIR and mid-IR regime.

**Funding.** H2020 European Research Council (787097).

**Acknowledgements.** We thank FIRST clean room facility at ETH Zurich.

**Disclosures.** The authors declare that there are no conflicts of interest related to this article.

#### References

1. U. Keller, K. J. Weingarten, F. X. Kärtner, D. Kopf, B. Braun, I. D. Jung, R. Fluck, C. Honninger, N. Matuschek, and J. Aus der Au, "Semiconductor saturable absorber mirrors (SESAM's) for femtosecond to nanosecond pulse generation in solid-state lasers," *IEEE J. Sel. Top. Quantum Electron.* **2**(3), 435–453 (1996).
2. U. Keller, "Ultrafast solid-state laser oscillators: A success story for the last 20 years with no end in sight," *Appl. Phys. B* **100**(1), 15–28 (2010).
3. I. T. Sorokina and K. L. Vodopyanov, *Solid-State Mid-Infrared Laser Sources* (Springer, 2003).
4. A. Godard, "Infrared (2–12  $\mu\text{m}$ ) solid-state laser sources: a review," *Comptes Rendus Phys.* **8**(10), 1100–1128 (2007).
5. S. Kivistö, T. Hakulinen, M. Guina, and O. G. Okhotnikov, "Tunable Raman soliton source using mode-locked Tm-Ho fiber laser," *IEEE Photonics Technol. Lett.* **19**(12), 934–936 (2007).
6. M. Guina, A. Härkönen, J. Paajaste, J.-P. Alanko, S. Suomalainen, C. Grebing, and G. Steinmeyer, "Passively mode-locked GaSb-based VECSELs emitting sub-400-fs pulses at 2  $\mu\text{m}$ ," *Proc. SPIE* **8242**, 824204 (2012).
7. J. Ma, Z. Qin, G. Xie, L. Qian, and D. Tang, "Review of mid-infrared mode-locked laser sources in the 2.0  $\mu\text{m}$  - 3.5  $\mu\text{m}$  spectral region," *Appl. Phys. Rev.* **6**(2), 021317 (2019).
8. S. M. Link, A. Klenner, M. Mangold, M. Golling, B. W. Tilma, and U. Keller, "Dual-comb modelocked lasers," *Opt. Express* **23**(5), 5521–5531 (2015).
9. S. M. Link, D. J. H. C. Maas, D. Waldburger, and U. Keller, "Dual-comb spectroscopy of water vapor with a free-running semiconductor disk laser," *Science* **356**(6343), 1164–1168 (2017).
10. J. Yu, M. Petros, U. N. Singh, T. F. Refaat, K. Reithmaier, R. G. Remus, and W. Johnson, "An airborne 2- $\mu\text{m}$  double-pulsed direct-detection lidar instrument for atmospheric CO<sub>2</sub> column measurements," *J. Atmos. Ocean. Technol.* **34**(2), 385–400 (2017).
11. I. E. Gordon, L. S. Rothman, C. Hill, R. V. Kochanov, Y. Tan, P. F. Bernath, M. Birk, V. Boudon, A. Campargue, K. V. Chance, B. J. Drouin, J. M. Flaud, R. R. Gamache, J. T. Hodges, D. Jacquemart, V. I. Perevalov, A. Perrin, K. P. Shine, M. A. H. Smith, J. Tennyson, G. C. Toon, H. Tran, V. G. Tyuterev, A. Barbe, A. G. Császár, V. M. Devi, T. Furtenbacher, J. J. Harrison, J. M. Hartmann, A. Jolly, T. J. Johnson, T. Karman, I. Kleiner, A. A. Kyuberis, J. Loos, O. M. Lyulin, S. T. Massie, S. N. Mikhailenko, N. Moazzen-Ahmadi, H. S. P. Müller, O. V. Naumenko, A. V. Nikitin, O. L. Polyansky, M. Rey, M. Rotger, S. W. Sharpe, K. Sung, E. Starikova, S. A. Tashkun, J. Vander Auwera, G. Wagner, J. Wilzewski, P. Wcislo, S. Yu, and E. J. Zak, "The HITRAN2016 molecular spectroscopic database," *J. Quant. Spectrosc. Radiat. Transfer* **203**, 3–69 (2017).
12. F. X. Kärtner, I. D. Jung, and U. Keller, "Soliton mode-locking with saturable absorbers," *IEEE J. Sel. Top. Quantum Electron.* **2**(3), 540–556 (1996).
13. F. X. Kärtner, J. Aus Der Au, and U. Keller, "Mode-locking with slow and fast saturable absorbers - What's the difference?" *IEEE J. Sel. Top. Quantum Electron.* **4**(2), 159–168 (1998).
14. R. Paschotta and U. Keller, "Passive mode locking with slow saturable absorbers," *Appl. Phys. B: Lasers Opt.* **73**(7), 653–662 (2001).
15. M. Haiml, R. Grange, and U. Keller, "Optical characterization of semiconductor saturable absorbers," *Appl. Phys. B* **79**(3), 331–339 (2004).
16. D. J. Maas, B. Rudin, A.-R. Bellancourt, D. Iwaniuk, S. V. Marchese, T. Südmeyer, and U. Keller, "High precision optical characterization of semiconductor saturable absorber mirrors," *Opt. Express* **16**(10), 7571–7579 (2008).

17. L. Orsila, A. Härkönen, J. Hytti, M. Guina, and G. Steinmeyer, "Ultrahigh precision nonlinear reflectivity measurement system for saturable absorber mirrors with self-referenced fluence characterization," *Opt. Lett.* **39**(15), 4384–4387 (2014).
18. K. Viskontas and N. Rusteika, "All-fiber wavelength-tunable picosecond nonlinear reflectivity measurement setup for characterization of semiconductor saturable absorber mirrors," *Opt. Fiber Technol.* **31**, 74–82 (2016).
19. A. Härkönen, J. Paajaste, S. Suomalainen, J.-P. Alanko, C. Grebing, R. Koskinen, G. Steinmeyer, and M. Guina, "Picosecond passively mode-locked GaSb-based semiconductor disk laser operating at 2 $\mu$ m," *Opt. Lett.* **35**(24), 4090–4092 (2010).
20. B. W. Tilma, M. Mangold, C. A. Zaugg, S. M. Link, D. Waldburger, A. Klenner, A. S. Mayer, E. Gini, M. Golling, and U. Keller, "Recent advances in ultrafast semiconductor disk lasers," *Light: Sci. Appl.* **4**(7), e310 (2015).
21. B. Willenberg, J. Pupekis, L. M. Krüger, F. Koch, C. R. Phillips, and U. Keller, "Femtosecond dual-comb Yb:CaF<sub>2</sub> laser from a single free-running polarization-multiplexed cavity for optical sampling applications," *Opt. Express* **28**(20), 30275–30288 (2020).
22. L. M. Krüger, A. S. Mayer, Y. Okawachi, X. Ji, A. Klenner, A. R. Johnson, C. Langrock, M. M. Fejer, M. Lipson, A. L. Gaeta, V. J. Wittwer, T. Südmeyer, C. R. Phillips, and U. Keller, "Performance scaling of a 10-GHz solid-state laser enabling self-referenced CEO frequency detection without amplification," *Opt. Express* **28**(9), 12755–12770 (2020).
23. J. Paajaste, S. Suomalainen, A. Härkönen, U. Griebner, G. Steinmeyer, and M. Guina, "Absorption recovery dynamics in 2 m GaSb-based SESAMs," *J. Phys. D: Appl. Phys.* **47**(6), 065102 (2014).
24. R. Grange, M. Haiml, R. Paschotta, G. J. Spühler, L. Krainer, M. Golling, O. Ostinelli, and U. Keller, "New regime of inverse saturable absorption for self-stabilizing passively mode-locked lasers," *Appl. Phys. B* **80**(2), 151–158 (2005).
25. C. J. Saraceno, C. Schriber, M. Mangold, M. Hoffmann, O. H. Heckl, C. R. E. Baer, M. Golling, T. Südmeyer, and U. Keller, "SESAMs for high-power oscillators: Design guidelines and damage thresholds," *IEEE J. Sel. Top. Quantum Electron.* **18**(1), 29–41 (2012).
26. I. J. Graumann, "Novel Approaches to Power Scale Ultrafast Thin-Disk Lasers at Short Pulse Durations," PhD thesis, ETH Zurich (2020).
27. E. W. Van Stryland, M. A. Woodall, H. Vanherzeele, and M. J. Soileau, "Energy band-gap dependence of two-photon absorption," *Opt. Lett.* **10**(10), 490–492 (1985).
28. M. D. Turner, W. B. Roh, and K. L. Schepler, "Nonlinear optical properties of GaSb and GaInAsSb and their application for phase conjugation in degenerate four-wave mixing," *J. Opt. Soc. Am. B* **17**(5), 790–804 (2000).
29. M. Grundmann, *The Physics of Semiconductors* (Springer International Publishing, 2016, p. 374).
30. D. J. H. C. Maas, A. R. Bellancourt, M. Hoffmann, B. Rudin, Y. Barbarin, M. Golling, T. Südmeyer, and U. Keller, "Growth parameter optimization for fast quantum dot SESAMs," *Opt. Express* **16**(23), 18646–18656 (2008).
31. R. Paschotta, R. Häring, A. Garnache, S. Hoogland, A. C. Tropper, and U. Keller, "Soliton-like pulse-shaping mechanism in passively mode-locked surface-emitting semiconductor lasers," *Appl. Phys. B: Lasers Opt.* **75**(4-5), 445–451 (2002).
32. P. C. Findlay, C. R. Pidgeon, H. Pellemans, R. Kotitschke, B. N. Murdin, T. Ashley, A. D. Johnson, A. M. White, and C. T. Elliott, "Auger recombination dynamics of InxGa1-xSb," *Semicond. Sci. Technol.* **14**(12), 1026–1030 (1999).